Testing (modified) gravity with 3D and tomographic cosmic shear

A. Spurio Mancini,[1]⋆ R. Reischke,[2] V. Pettorino,[3] B. M. Schäfer[2] and M. Zumalacárregui[4,5]

[1]*Institut für Theoretische Physik, Heidelberg Universität, Philosophenweg 12, D-69120 Heidelberg, Germany*
[2]*Astronomisches Rechen-Institut, Zentrum für Astronomie der Universität Heidelberg, Philosophenweg 12, D-69120 Heidelberg, Germany*
[3]*AIM, CEA, CNRS, Université Paris-Saclay, Université Paris Diderot, Sorbonne Paris Cité, F-91191 Gif-sur-Yvette, France*
[4]*Berkeley Center for Cosmological Physics, LBNL and University of California at Berkeley, Berkeley, 94720 California, USA*
[5]*Institut de Physique Théorique, CEA, Université Paris-Saclay, CNRS, F-91191 Gif-sur-Yvette, France*

ABSTRACT

Cosmic shear is one of the primary probes to test gravity with current and future surveys. There are two main techniques to analyse a cosmic shear survey: a tomographic method, where correlations between the lensing signals in different redshift bins are used to recover redshift information, and a 3D approach, where the full redshift information is carried through the entire analysis. Here we compare the two methods, by forecasting cosmological constraints for future surveys like Euclid. We extend the 3D formalism for the first time to theories beyond the standard model, belonging to the Horndeski class. This includes the majority of universally coupled extensions to ΛCDM with one scalar degree of freedom in addition to the metric, still in agreement with current observations. Given a fixed background, the evolution of linear perturbations in Horndeski gravity is described by a set of four functions of time only. We model their time evolution assuming proportionality to the dark energy density fraction and place Fisher matrix constraints on the proportionality coefficients. We find that a 3D analysis can constrain Horndeski theories better than a tomographic one, in particular with a decrease in the errors of the order of 20 per cent. This paper shows for the first time a quantitative comparison on an equal footing between Fisher matrix forecasts for both a fully 3D and a tomographic analysis of cosmic shear surveys. The increased sensitivity of the 3D formalism comes from its ability to retain information on the source redshifts along the entire analysis.

Key words: gravitational lensing: weak – dark energy – large-scale structure of Universe.

1 INTRODUCTION

The observed acceleration of the Universe (Riess et al. 1998; Perlmutter et al. 1999) can be ascribed to a dark energy component accounting for approximately 70 per cent of the energy budget of the Universe. From a theoretical point of view, identifying the dark energy with a cosmological constant term Λ fits well the observations, but has been questioned in terms of naturalness and interpretation in terms of energy density of the vacuum (see Martin 2012 for a recent review). Alternatives to the cosmological constant can be generally grouped into two main categories. Either dark energy is a modification of gravity on the largest scales ('modified gravity' theories), or it is given by a scalar field that effectively behaves as a fluid with negative pressure (usually referred to as proper 'dark energy' models). The distinction between these two classes can at times be feeble (see Joyce, Lombriser & Schmidt 2016 for a recent

discussion) and the vast amount of proposed theories (see Clifton et al. 2012 for a review) urgently calls for methods to be developed, aiming at distinguishing among the large number of theoretical options with advanced statistical methods and efficient computational effort. This is particularly relevant in light of the unprecedented amount of data that will come from many space- and ground-based experiments, such as *Euclid*,[1] SKA[2] (Maartens et al. 2015), LSST[3] (LSST Science Collaboration 2009), and *WFIRST*[4] (Spergel et al. 2013), whose launch in the next few years is planned with the goal of unveiling the true nature of the cosmic acceleration.

The Horndeski class of modified gravity theories represent an example of a remarkably large set of extensions to General Relativity. First discussed in 1974 by Horndeski (Horndeski 1974) and subsequently rediscovered in Nicolis, Rattazzi, and Trincherini (2009)

⋆ E-mail: spuriomancini@thphys.uni-heidelberg.de

[1] https://www.euclid-ec.org/
[2] https://www.skatelescope.org/
[3] https://www.lsst.org/
[4] https://wfirst.gsfc.nasa.gov/

and Deffayet et al. (2011), the Horndeski Lagrange density is the most general gravitational theory with one scalar degree of freedom, in addition to the metric tensor, with derivatives in the equations of motion not higher than second order; this guarantees safety from ghost-like degrees of freedom. This set of theories collects under its name many different models of dark energy/modified gravity (see Section 2 for a list of some of these). Theories that contain higher order derivatives but are still free from ghost degrees of freedom, belong to the 'Beyond Horndeski' category (Zumalacárregui & García-Bellido 2014; Gleyzes et al. 2015; Crisostomi & Koyama 2017; Langlois et al. 2017).

On the observational side, many different probes have been proposed to investigate dark energy/modified gravity models. These include type Ia Supernovae, baryon acoustic oscillations, galaxy clustering, and weak gravitational lensing, to name a few (see e.g. Weinberg et al. 2013 for an exhaustive review of the different probes). In this paper we focus on the weak gravitational lensing caused by the large-scale structure of the Universe, or cosmic shear. Since the first detections in early 2000s (e.g. Bacon, Refregier & Ellis 2000; Van Waerbeke et al. 2000; Brown et al. 2003), this field has developed within a well-established theoretical and experimental framework. Cosmic shear is particularly appealing as one of the most promising probes of dark energy (Jain & Taylor 2003; Bernstein & Jain 2004; Hannestad, Tu & Wong 2006; Amendola, Kunz & Sapone 2008; Huterer 2010); the differential deflection in light bundles from distant galaxies caused by variations of the gravitational fields of the large-scale structure result in a coherent distortion of galaxy images as we observe them on the sky (see Bartelmann & Schneider 2001; Hoekstra & Jain 2008; Kilbinger et al. 2013, for reviews on the topic). Thus cosmic shear is sensitive to the growth rate of the perturbations of the gravitational potential and to the geometry of the Universe through the distance–redshift relation. These features are crucial for dark energy studies, as they allow us to measure how the expansion rate and growth of structure change with time: It follows that the sensitivity of cosmic shear to dark energy can be fully exploited if the analysis performed is able to recover information on the evolution in redshift of the large-scale structure. This is only to a little extent achieved in a 2D analysis: galaxy shapes are observed on the 2D celestial sphere and the shear components are line-of-sight projected quantities, with the projection causing loss of information on the redshift evolution (Jain & Seljak 1997; Takada & Jain 2003a,b; Munshi & Kilbinger 2006; Jee et al. 2013; Kilbinger et al. 2013). For this reason, as an alternative to a pure 2D projection, a tomographic analysis based on a binning in redshift of the sources has been first proposed in Hu (1999) and has since become the standard technique for cosmological weak lensing studies (Simon, King & Schneider 2004; Takada & Jain 2004; Takada & White 2004; Hollenstein et al. 2009; Kilbinger et al. 2009; Schäfer & Heisenberg 2012; Heymans et al. 2013). Galaxies are assigned to different bins according to their redshifts, so that intra and interbin correlations of the binned shear field can be computed. This reduces the range of the projection to the width of the bins and allows for some gain in redshift information through the interbin correlations. Despite its success in providing some sensitivity to the growth of structure with its '2D$\frac{1}{2}$' nature, as it has sometimes been relabelled, tomography has still the disadvantage of representing a compression of data: The 2D analysis performed within a single bin is such that the range of the projection is smaller than in the pure 2D case, being restricted to the width of the bin, however, this does not represent yet a fully 3D treatment of the shear field.

As an alternative to tomography, a method to retain information on the redshift of each source galaxy along the entire weak lensing analysis has been first proposed in Heavens (2003) and subsequently refined in Castro, Heavens, and Kitching (2005); Heavens, Kitching, and Taylor (2006); Kitching, Heavens, and Miller (2011). Based on a spherical Fourier–Bessel decomposition of the shear field, it is immune from the aforementioned approximations presented in (Kitching et al. 2016a). In addition to avoiding any binning and averaging in redshift, the spherical Fourier–Bessel formalism allows for a separation of angular (ℓ) and radial (k) modes (Kitching et al. 2014); the fact that they can be treated independently makes it easier than in tomography to reduce the impact of problematic small scales, where models for the non-linear growth of structure (Smith et al. 2003; Takahashi et al. 2012; Mead et al. 2015), or baryon feedback (Semboloni et al. 2011; van Daalen et al. 2011; Semboloni, Hoekstra & Schaye 2013) do not yet provide a fully reliable description. These advantages compensate for the extra computational time required by the more complicated integrations in the covariance of the shear modes. To date, the 3D weak lensing approach has been applied to real data only in Kitching et al. (2007, 2014, 2016b) for a ΛCDM model. Grassi and Schäfer (2014) investigated the possibility of detecting baryon acoustic oscillation features in the cosmic matter distribution by 3D weak lensing; Zieser and Merkel (2016) studied the cross-correlation between the 3D weak lensing signal and the integrated Sachs–Wolfe effect; Camera et al. (2011) investigated the constraining power of 3D cosmic shear on a class of unified dark matter models, where a single scalar field mimics both dark matter and dark energy, whereas Ayaita, Schäfer, and Weber (2012) employed 3D cosmic shear to explore the capability of future surveys to constrain dark energy clustering. While 3D weak lensing has been partially studied in the context of modified gravity theories in Pratten et al. (2016) to constrain $f(R)$ chameleon models and environmentally dependent dilation models, showing that for an all-sky spectroscopic survey the $f(R)$ parameter f_{R_0} can be constrained in the range $f_{R_0} < 5 \times 10^{-6}(9 \times 10^{-6})$ for $n = 1(2)$ with a 3σ confidence level, there has not been any application to a larger class of modified gravity theories. Alonso et al. (2016) forecast the sensitivity of future surveys to Horndeski theories using different probes, among which there is tomographic weak lensing.

In this paper we propose for the first time the 3D cosmic shear as a probe of Horndeski theories of modified gravity. We analyse in detail the expected performance of a Euclid-like experiment, with the aim of forecasting the precision with which future stage IV surveys will be able to constrain this class of alternatives to general relativity using cosmic shear data sets. We choose the parametrization of linear perturbations in Horndeski gravity first proposed by Bellini and Sawicki (2014) and based on four functions of time only, which completely describe the evolution of linear perturbations once the background evolution is fixed. We model their time evolution assuming proportionality to the density fraction of dark energy and constrain the proportionality coefficients under the assumption of Gaussian likelihood. We simultaneously also place constraints on a set of standard cosmological parameters describing the evolution of the background, including the sum of the neutrino masses.

We produce our forecasts for both a fully 3D and a tomographic analysis of the measurements with the aim of comparing the performances of the two methods on both modified gravity and standard cosmological parameters. Kitching et al. (2011) showed the relationship between weak lensing tomography and the 3D cosmic shear field, connected by the Limber approximation, a harmonic-space transform and a discretization in wavenumber. Our work presents for the first time a quantitative comparison on an equal footing between 3D and tomographic techniques for cosmic shear in terms of Fisher forecasts, showing that the 3D approach has more

sensitivity than tomography to both standard and modified gravity cosmological parameters. We vary both the background cosmological parameters and those describing Horndeski theories, and consider only weak gravitational lensing as a cosmological observable, to test its power in constraining modified gravity theories without other probes and compare 3D and tomographic methodologies.

This article is structured as follows: in Section 2 we review the Horndeski Lagrangian and introduce the Bellini and Sawicki (2014) parametrization; in Section 3 we present both the spherical Fourier–Bessel formalism for 3D weak lensing and the tomographic approach in a modified gravity context; in Section 4 we explain our Fisher matrix analysis and report the specifications of the Euclid-like survey we consider; in Section 5 we present our Fisher forecasts for both 3D and tomographic cosmic shear; in Section 6 we draw conclusions from our analysis.

2 HORNDESKI THEORIES

The Horndeski Lagrange density (Horndeski 1974) is the most general way of writing the Lagrangian of a scalar–tensor theory of gravity that is 4D, Lorentz-invariant, local, and has equations of motion with derivatives not higher than second order. This ensures the safety of the theory against Ostrogradski instabilities and subsequent ghost degrees of freedom (Woodard 2007). The Horndeski action can be written as follows:

$$S[g_{\mu\nu}, \phi] = \int d^4x \sqrt{-g} \left[\sum_{i=2}^{5} \frac{1}{8\pi G_N} \mathcal{L}_i[g_{\mu\nu}, \phi] + \mathcal{L}_m[g_{\mu\nu}, \psi_M] \right],$$

$$\mathcal{L}_2 = G_2(\phi, X),$$

$$\mathcal{L}_3 = -G_3(\phi, X)\Box\phi,$$

$$\mathcal{L}_4 = G_4(\phi, X)R + G_{4X}(\phi, X)\left[(\Box\phi)^2 - \phi_{;\mu\nu}\phi^{;\mu\nu}\right],$$

$$\mathcal{L}_5 = G_5(\phi, X)G_{\mu\nu}\phi^{;\mu\nu}$$
$$- \frac{1}{6}G_{5X}(\phi, X)\left[(\Box\phi)^3 + 2\phi_{;\mu}{}^\nu\phi_{;\nu}{}^\alpha\phi_{;\alpha}{}^\mu \right.$$
$$\left. - 3\phi_{;\mu\nu}\phi^{;\mu\nu}\Box\phi\right]. \tag{1}$$

The four contributions $\mathcal{L}_i$ of the gravitational sector depend on arbitrary functions of the metric $g_{\mu\nu}$ and the kinetic term $K = -\frac{1}{2}\partial_\mu\phi\partial^\mu\phi$ of the additional scalar degree of freedom ϕ. The subscripts ϕ, X denote partial derivatives, e.g. $G_{iX} = \frac{\partial G_i}{\partial X}$. We write the normalization of the G_i functions following the convention implemented in the HI_CLASS code (Zumalacárregui et al. 2016). We will consider only universal coupling between the metric and the matter fields (collectively described by ψ_m and contained in the matter Lagrangian $\mathcal{L}_m$), which are therefore uncoupled to the scalar field. Most of the universally coupled models with one scalar degree of freedom belong to the Horndeski class. These include for example quintessence (Ratra & Peebles 1988; Wetterich 2009), Brans–Dicke models (Brans & Dicke 1961), k-essence (Armendáriz-Picón, Damour & Mukhanov 1999; Armendariz-Picon, Mukhanov & Steinhardt 2001), kinetic gravity braiding (Deffayet et al. 2010; Kobayashi, Yamaguchi & Yokoyama 2010; Pujolàs, Sawicki & Vikman 2011), covariant galileons (Deffayet, Esposito-Farèse & Vikman 2009; Nicolis et al. 2009), disformal and Dirac–Born–Infeld gravity (de Rham & Tolley 2010; Bettoni & Liberati 2013; Zumalacárregui, Koivisto & Mota 2013), Chameleons (Khoury & Weltman 2004a; Khoury & Weltman 2004b), symmetrons (Hinterbichler & Khoury 2010; Hinterbichler et al. 2011), Gauss–Bonnet couplings (Ezquiaga, García-Bellido & Zumalacárregui 2016) and models screening the cosmological constant (Charmousis et al. 2012; Martín-Moruno, Nunes & Lobo 2015). Archetypal modified

gravity-models such as all variants of *f(R)* (Carroll et al. 2004) and *f(G)* (Carroll et al. 2005) theories are also included. Models that are not within this broad class are those that contain higher derivatives in the equations of motion (Zumalacárregui & García-Bellido 2014; Gleyzes et al. 2015), and modifications of gravity with non-scalar degrees of freedom, e.g. Einstein–Aether models (Jacobson & Mattingly 2001) or ghost-free massive gravity (de Rham & Gabadadze 2010; de Rham, Gabadadze & Tolley 2011; Hassan & Rosen 2012). The choice of the $G_i(g_{\mu\nu}, K)$ functions completely specifies the single modified gravity model that one considers.

When dealing with linear perturbations acting on a Friedmann–Robertson–Walker metric in modified gravity, one can assume spatial flatness, and considering only scalar perturbations (see Adamek, Durrer & Tansella 2016; Durrer & Tansella 2016, for vector and tensor perturbations), write the line element in Newtonian gauge as

$$ds^2 = -\left(1 + 2\frac{\Phi}{c^2}\right)c^2 dt^2 + a^2(t)\left(1 - 2\frac{\Psi}{c^2}\right)d\mathbf{x}^2, \tag{2}$$

with the Bardeen potentials Φ and Ψ. In General Relativity $\Phi = \Psi$ in absence of anisotropic stress, while this is in general not true in modified gravity. In Gleyzes et al. (2013) and Bellini AND Sawicki (2014), it has been shown that one can parametrize the evolution of linear cosmological perturbations in Horndeski theories by means of four functions of (conformal) time only, which we will collectively refer to here as α functions. Each of them carries a physical meaning, which we describe briefly here, referring to Bellini and Sawicki (2014) and references therein for a more complete description:

(i) α_K is the *kineticity* term, i.e. the kinetic energy of the scalar perturbations arising directly from the action. Increasing this term suppresses the sound speed of scalar perturbations. This makes the sound horizon smaller than the cosmological horizon, allowing the scalar field to enter a quasi-static configuration on smaller scales, below the sound horizon (Sawicki & Bellini 2015). In the quasi-static approximation where time derivatives are considered to be sub-dominant with respect to space derivatives, α_K does not enter the equations of motion, and is therefore largely unconstrained by cosmic shear (Alonso et al. 2016; Bellini et al. 2016, although see Kreisch and Komatsu 2017).

(ii) α_B is the *braiding* term which describes mixing of the scalar field with the metric kinetic term, leading to what is typically interpreted as a fifth force between massive particles.

(iii) α_M is the *Planck-mass run rate*, defined by

$$\alpha_M \equiv \frac{d \ln M_*^2}{d \ln a}, \tag{3}$$

where M_*^2 is the dimensionless product of the normalization of the kinetic term for gravitons and $8\pi G_N$ measured on Earth. This function describes the rate of evolution of the effective Planck mass.

(iv) α_T is the *tensor speed excess,* indicating deviations from the speed of light in the propagation speed of gravitational waves. This can lead to anisotropic stress even in the absence of scalar field perturbations, as a result of a change in the response of the Newtonian potential to matter sources. Recently, very strong constraints have been placed on α_T by the measurement of the gravitational waves speed derived by the detection of the binary neutron star merger GW170817 and the gamma ray burst GRB170817A (Abbott et al. 2017a,b; Baker et al. 2017; Bettoni et al. 2017; Creminelli & Vernizzi 2017; Ezquiaga & Zumalacárregui 2017; Lombriser & Lima 2017; Sakstein & Jain 2017). Since the speed has been found to be very close to the speed of light, α_T has been consequently constrained to be very close to zero at the present

time. We remark that the other three functions (as well as α_T's past value), are instead still free to vary. Ezquiaga and Zumalacárregui (2017) identify the models within the Horndeski classes that are still viable after GW170817; Peirone et al. (2018) show that even with the strict bound on the present-day gravitational wave speed, there is still room within Horndeski theories for non-trivial signatures of modified gravity, which can be measured at the level of linear perturbations.

The specific model considered within the Horndeski class is defined by the choice of the α_i functions. The ΛCDM model corresponds to the choice $\alpha_K = \alpha_B = \alpha_M = \alpha_T = 0$. Once the α functions are set, Bellini and Sawicki (2014) show that it is sufficient to solve the equations of motion for the background and perturbations to fully determine the evolution of linear perturbations at the linear level.

In this paper, we aim at forecasting constraints on the α functions with a Fisher matrix analysis for a cosmic shear survey. In doing so, we need to choose a parametrization for the time evolution of the α functions. Following a common procedure, already implemented in HI_CLASS, we choose to parametrize these functions, such that they trace the evolution of the dark energy component to which they are proportional,

$$\alpha_i = \hat{\alpha}_i \, \Omega_{\mathrm{DE}}(\tau). \tag{4}$$

This choice, first suggested in Bellini and Sawicki (2014), is the simplest and the most common in the literature (as used e.g. in Planck Collaboration XIV 2016) and, despite not being the only one, can already provide a lot of information on Horndeski gravity, as remarked by Gleyzes (2017), who showed that simple parametrizations are sufficient to describe the theory space in effective field theory of dark energy (Gubitosi, Piazza & Vernizzi 2013; Gleyzes et al. 2015), which the Bellini and Sawicki (2014) parametrization belongs to. The forecasts we present in Section 5 will therefore be on the proportionality coefficients $\hat{\alpha}_i$.

3 COSMIC SHEAR

3.1 3D cosmic shear

Weak gravitational lensing of the large-scale structure in the Universe is the deflection of light rays coming from distant sources due to the distortion of the cross-sectional shape of light bundles (see Bartelmann & Schneider 2001; Hoekstra & Jain 2008; Kilbinger 2015, for reviews on the topic). The typical lensing signal is a distortion or shear of the source image due to the gravitational potential generated by the mass distribution between the source and the observer. Cosmic shear measurements are of statistical nature, as the lensing effect is not associated with a particular intervening lens, but rather corresponds to small distortions (of the order of 1 per cent) by all density fluctuations along the line of sight. The statistical properties of the shear reflect those of the underlying density field and a particularly informative insight is given in configuration space by the two-point statistics or correlation function of the shear field.

We present here a general formalism for a fully 3D expansion of the shear field that does not perform any binning in redshift. This is based on a spherical Fourier–Bessel decomposition of the shear, first introduced in lensing studies by Heavens (2003). Here we follow the notation and conventions of Zieser and Merkel (2016) and extend the presentation given there to a general modified gravity scenario characterized by the Bardeen potentials Φ and Ψ defined in (2).

Information on the gravitational potential is encoded in a weighted projection along the line of sight, the lensing potential. In a modified gravity context, considering perturbations at the linear level, the lensing potential ϕ is related to the Bardeen potentials Ψ and Φ by

$$\phi(\chi, \hat{\mathbf{n}}) = \int_0^\chi \mathrm{d}\chi' \frac{\chi - \chi'}{\chi \chi'} \frac{\Phi(\chi, \hat{\mathbf{n}}) + \Psi(\chi, \hat{\mathbf{n}})}{c^2}, \tag{5}$$

where χ is a comoving distance, and the normalized vector $\hat{\mathbf{n}}$ selects a direction on the sky. Here and throughout the paper, spatial flatness will be assumed and the integration in (5) is carried out in Born approximation, i.e. along the unperturbed light path. The shear tensor $\gamma(\chi, \hat{\mathbf{n}})$ is defined as the second $\eth$-derivative (Newman & Penrose 1962; Goldberg et al. 1967) of the lensing potential (Heavens 2003; Castro et al. 2005)

$$\gamma(\chi, \hat{\mathbf{n}}) = \frac{1}{2} \eth \eth \phi(\chi, \hat{\mathbf{n}}). \tag{6}$$

The $\eth$-derivative acts as a covariant differentiation operator on the celestial sphere and relates quantities of different spin, raising the spin s of a function, a number which characterizes its transformation properties under rotations. Acting twice on ϕ, the $\eth$ operator relates the scalar (spin-0) lensing potential to the spin-2 shear field γ. The shear γ can be expanded with a choice of basis functions given by a combination of spherical Bessel functions $j_\ell(z)$ (Abramowitz, Stegun & Romer 1988) and spin 2-weighted spherical harmonics $_2Y_{\ell m}(\hat{\mathbf{n}})$

$$\gamma(\chi, \hat{\mathbf{n}}) = \sqrt{\frac{2}{\pi}} \sum_{\ell m} \int k^2 \, \mathrm{d}k \, \gamma_{\ell m}(k) \, _2Y_{\ell m}(\hat{\mathbf{n}}) \, j_\ell(k\chi), \tag{7}$$

where the coefficients $\gamma_{\ell m}(k)$ are given by

$$\gamma_{\ell m}(k) = \sqrt{\frac{2}{\pi}} \int \chi^2 \mathrm{d}\chi \int \mathrm{d}\Omega \, \gamma(\chi, \hat{\mathbf{n}}) \, j_\ell(k\chi) \, _2Y_{\ell m}^*(\hat{\mathbf{n}}). \tag{8}$$

Inserting (5) and (6) in (8), and applying a spherical Fourier–Bessel expansion to the Bardeen potentials Φ and Ψ, we can rewrite γ as

$$\gamma(\chi, \hat{\mathbf{n}}) = \sqrt{\frac{2}{\pi}} \frac{1}{c^2} \int_0^\chi \mathrm{d}\chi' \frac{\chi - \chi'}{\chi \chi'} \int k^2 \mathrm{d}k \sum_{\ell m} \sqrt{\frac{(\ell + 2)!}{(\ell - 2)!}}$$
$$\times \left[\frac{\Phi_{\ell m}(k, \chi') + \Psi_{\ell m}(k, \chi')}{2} \right] j_\ell(k\chi') \, _2Y_{\ell m}(\hat{\mathbf{n}}), \tag{9}$$

where the division by 2 comes from the pre-factor in (6).

Poisson's equation can be used to link the coefficients in the spherical Fourier–Bessel decomposition of the lensing potential to those of the overdensity field $\delta_{\ell m}(k, \chi)$,

$$\frac{\Phi_{\ell m}(k, \chi)}{c^2} = -\frac{3}{2} \frac{\Omega_m}{(k\chi_H)^2} \frac{\delta_{\ell m}(k, \chi)}{a(\chi)} \mu(k, a(\chi)), \tag{10}$$

with the Hubble radius $\chi_H \equiv c/H_0$. Here the function $\mu(k, a(\chi))$ describes the mapping from the potential fluctuations to the density fluctuations. Equation (10) can also be used as a parametrization of modified gravity theories (e.g. Planck Collaboration XIV 2016). The latter approach, however, only holds in the quasi-static regime, where one neglects terms involving time derivatives in the Einstein equations for perturbations and keeps only spatial derivatives (Sawicki & Bellini 2015; Baker & Bull 2015). For the Euclid survey, it could be questionable if this approximation holds, given the large scales in principle accessible by the survey. The validity of the quasi-static approximation depends also on the single modified gravity model considered and its predictions for the sound speed of the additional scalar degree of freedom. That said, we stress that

we are not using this parametrization, but rather take the potential and density statistics directly from HI_CLASS, which does not use the quasi-static approximation.

The density field is statistically homogeneous and isotropic, characterized by a power spectrum which is diagonal in harmonic space,

$$\langle \delta_{lm}(k, z)\delta^*_{\ell'm'}(k', z')\rangle = \frac{P_\delta(k, z, z')}{k^2}\delta^D(k - k')\delta^K_{\ell\ell'}\delta^K_{mm'}. \quad (11)$$

Using this, we can relate the covariance of shear modes to the matter power spectrum by

$$\langle \bar{\gamma}_{lm}(k)\bar{\gamma}^*_{\ell'm'}(k')\rangle = \frac{9\Omega^2_m}{16\pi^4\chi^4_H}\frac{(\ell+2)!}{(\ell-2)!}$$

$$\times \int \frac{d\tilde{k}}{\tilde{k}^2}\, G_\ell(k, \tilde{k})\, G_\ell(k', \tilde{k})\, \delta^K_{\ell\ell'}\, \delta^K_{mm'}, \quad (12)$$

where

$$G_\ell(k, k') = \int dz\, n_z(z)\, F_\ell(z, k)\, U_\ell(z, k'), \quad (13)$$

$$F_\ell(z, k) = \int dz_p\, p(z_p|z)\, j_\ell[k\chi^0(z_p)], \quad (14)$$

$$U_\ell(z, k) = \frac{1}{2}\int^{\chi(z)}_0 \frac{d\chi'}{a(\chi')}\frac{\chi - \chi'}{\chi\chi'}\, j_\ell(k\chi')\, P^{1/2}_\delta(k, z(\chi))$$

$$\times \mu(k, a(\chi))\left[1 + \frac{1}{\eta(k, a(\chi'))}\right]. \quad (15)$$

$\bar{\gamma}$ are estimates of the shear modes that, in addition to the pure lensing effect, keep into account the redshift distribution of galaxies and the redshift estimation error (see Section 4.2 for details on observational effects), as evidenced by the definition of the quantities in (13), (14), and (15), which contain the redshift distribution $n_z(z)$ of the lensed galaxies and the conditional probability $p(z_p|z)$ of estimating the redshift z_p, given the true redshift z. These two elements and the lensing kernel contained in the function $U_\ell(z, k)$ introduce correlations between the amplitudes of the signal on different scales; the covariance matrix then acquires off-diagonal terms, the calculation of which is numerically involved. The basis of spherical Bessel functions leads to integrals with rapidly oscillatory kernels, which have to be solved for a large number of parameter combinations. $\eta(k, a(\chi'))$ is defined as the ratio between the Bardeen potentials,

$$\eta(k, a(\chi)) = \frac{\Phi(k, a(\chi))}{\Psi(k, a(\chi))}. \quad (16)$$

The $P^{1/2}_\delta(k, z(\chi))$ term comes from an approximation, introduced and justified in Castro et al. (2005) to calculate unequal-time correlators appearing in the comoving distance integrations by means of a geometric mean $P(k, z, z') \simeq \sqrt{P(k, z)\, P(k, z')}$ (see also Kitching & Heavens 2017). This expression simplifies considerably in the linear regime of structure formation, retrieving the one presented in the seminal paper of Heavens (2003), where a product of the linear growth factors at different redshifts is present, acting on the matter power spectrum evaluated at the present time.

The noise term for the covariance matrix of the shear modes is given by the intrinsic ellipticity dispersion of source galaxies as a result of the fact that the observed ellipticity ε is assumed to be the sum of the shear γ and the intrinsic ellipticity ε_S. The intrinsic ellipticity dispersion is given by $\langle \epsilon^2_S \rangle = \sigma^2_\epsilon$. In the spherical

Fourier–Bessel formalism, this gives

$$\langle \gamma_{\ell m}(k)\, \gamma_{\ell'm'}(k')\rangle_{SN} = \frac{\sigma^2_\epsilon}{2\pi^2}\int dz\, n_z(z)\, j_\ell[k\chi_0(z)]\, j_{\ell'}[k'\chi_0(z)]$$

$$\times \delta^K_{\ell\ell'}\delta^K_{mm'}, \quad (17)$$

and we set $\sigma_\varepsilon = 0.3$. This expression for the noise holds only in absence of intrinsic alignments, i.e. assuming that the intrinsic ellipticities of galaxies are uncorrelated (see Merkel & Schäfer 2013 for a study of intrinsic alignments in 3D weak lensing).

3.2 Tomography

Instead of keeping track of the photometric redshift error, as done in the 3D approach, by means of the probability $p(z_p|z)$ of estimating the redshift z_p conditional on the true redshift z, another possibility is to assign every galaxy to a redshift bin. In this case, as opposed to (12), the flat-sky tomographic cosmic shear power spectrum in tomographic bins i and j is given by

$$C^\kappa_{ij}(\ell) = \int \frac{d\chi}{\chi^2}\, W_i(\ell/\chi, \chi)W_j(\ell/\chi, \chi)\, P_\delta(\ell/\chi, \chi), \quad (18)$$

where we used the Limber projection. The lensing efficiency function $W_i(\ell/\chi, \chi)$ is defined as

$$W_i(\ell/\chi, \chi) = \frac{3\Omega_m}{4\chi^2_H}\int^\infty_\chi d\chi'\frac{dz}{d\chi'}\frac{n_i(z(\chi'))}{a(\chi')}\frac{\chi - \chi'}{\chi\chi'}$$

$$\times \left(1 + \frac{1}{\eta(\ell/\chi, \chi')}\right)\mu(\ell/\chi, \chi'), \quad (19)$$

where $n_i(z(\chi))$, being the distance distribution of sources in the i-th bin, which is normalized to one, $\int d\chi\, n_i(z(\chi)) = 1$. Observed spectra suffer from Poissonian noise due to the intrinsic ellipticity dispersion of galaxies σ_ε and their finite number n_0. Choosing our tomographic bins so as to have equal number of galaxies in each of them, the observed tomographic weak lensing spectrum is given by

$$\hat{C}^\kappa_{ij}(\ell) = C^\kappa_{ij}(\ell) + \frac{\sigma^2_\epsilon\, n_{bins}}{n_0}\delta_{ij}. \quad (20)$$

It should be noticed that comparing tomographic and 3D lensing must be done with some care since some approximations enter in (18). In particular, we made use of the flat-sky approximation and the Limber projection (Kaiser 1992, 1998; Loverde & Afshordi 2008), neither of which is included in the 3D formalism. For a detailed discussion on this we refer to Kitching et al. 2016a; Kilbinger et al. 2017; Lemos, Challinor & Efstathiou 2017, for an excellent discussion of various approximations performed in cosmic shear analyses.

4 METHODOLOGY

4.1 Fisher matrix forecasts

In order to present forecasts for a Euclid-like experiment on the parameters considered, we perform a Fisher matrix analysis (Tegmark, Taylor & Heavens 1997). Provided that the likelihood surface near the maximum is well approximated by a multivariate Gaussian, the Fisher matrix gives a realistic expectation of the foreseen error for a given experimental setting. The Fisher matrix is defined as the expectation value of the derivative of the logarithmic likelihood $\mathcal{L}$ with respect to the parameters θ_α:

$$F_{\alpha\beta} \equiv -\left\langle \frac{\partial^2\ln\mathcal{L}}{\partial\theta^\alpha\partial\theta^\beta}\right\rangle, \quad (21)$$

evaluated at the maximum of the log-likelihood $\mathcal{L}$, which in a forecast analysis coincides with the reference fiducial model. Once we have the Fisher matrix, the Cramer-Rao bound $\Delta\theta_\alpha^2 \geq (\boldsymbol{F}^{-1})_{\alpha\alpha}$ gives a lower limit on the expected marginal error on the parameter θ_α. If the data are Gaussian distributed and the mean values vanish, the Fisher matrix can be calculated from the covariance matrix and its derivatives with respect to the parameters (Tegmark et al. 1997)

$$F_{\alpha\beta} = \frac{1}{2}\text{Tr}\left[\boldsymbol{C}^{-1}\boldsymbol{C}_{,\alpha}\boldsymbol{C}^{-1}\boldsymbol{C}_{,\beta}\right]. \tag{22}$$

where derivatives have been denoted with a comma. Assuming full-sky coverage this expression can be simplified for a 3D weak lensing survey, as modes with different ℓ and m are uncorrelated ($\delta_{\ell\ell'}^K\delta_{mm'}^K$ in 12), leading to

$$F_{\alpha\beta} = \frac{1}{2}\sum_\ell (2\ell+1)\text{Tr}\left[\boldsymbol{C}_\ell^{-1}\boldsymbol{C}_{\ell,\alpha}\boldsymbol{C}_\ell\boldsymbol{C}_{\ell,\beta}\right], \tag{23}$$

as there are $2\ell+1$ statistically independent m modes for each ℓ. Note that expressions (22) and (23) are only exact if the data, in this case the modes $\gamma_{\ell m}(k)$, follow a Gaussian distribution. This is not the case for high-ℓ values, where structures due to non-linear clustering dominate the lensing signal (for a discussion on non-Gaussian statistics of the weak lensing field see e.g. Taruya et al. 2002; Joachimi, Taylor & Kiessling 2011; Clerkin et al. 2017). However, for the purpose of this paper this assumption will not be of any harm since the basic parameter dependencies are captured well enough within this approximation.

4.2 Observational effects and specifications

A 3D weak lensing analysis depends crucially on redshift estimation of the source galaxies, which for next generation surveys like *Euclid* (Laureijs et al. 2011) will be achieved using photometry, being the number of sources prohibitively high for spectroscopy. The estimated shear modes in (12) keep into account two observational effects, which are inherent in a redshift survey. The first one is described by the quantity G in (13) and represents the distribution in redshift of the galaxies, mainly due to the fact that they become fainter as redshift increases. For the source distribution we follow (Amendola et al. 2016) and choose in (13)

$$n_z(z) \propto n_0 \left(\frac{\sqrt{2}}{z_m}\right)^3 z^2 \exp\left[-\left(\frac{\sqrt{2}z}{z_m}\right)^{3/2}\right], \tag{24}$$

where z_m is the median redshift of the survey and n_0 is the observed redshift-integrated source density n_0. The second observational effect, kept into account in the quantity F in (14), is the error associated to redshift estimation. This is described by the probability of estimating the redshift z_p given the measured redshift z. We take this probability distribution to be a Gaussian

$$p(z_p|z) = \frac{1}{\sqrt{2\pi}\sigma(z)} \exp\left[-\frac{(z_p-z)^2}{2\sigma^2(z)}\right], \tag{25}$$

with a redshift-dependent dispersion

$$\sigma(z) = \sigma_z(1+z). \tag{26}$$

If the sky coverage is not complete then (23) is not completely correct, since the spherical basis is no longer orthogonal. None the less, (23) is a good approximation by just multiplying the right hand side with the sky-fraction $f_{sky} = \Omega_{survey}/\Omega_{sky}$. The choice we make for the specifications used in the analysis is summarized in Table 1.

Table 1. Specifications used in the Fisher matrix analysis for the Euclid survey: the median redshift z_m; the source density n_0; the error in photometric redshifts, $\sigma(z) = \sigma_z(1+z)$; the field size Ω_{sky}. ℓ_{min}, ℓ_{max}, and k_{max} describe instead the minimum and maximum radial modes and the maximum angular mode, respectively, considered in the computation of the shear covariances (12) and the Fisher matrix (23). n_{bins} is the number of bins considered in the tomographic analysis.

z_m	$n_0[\text{arcmin}^{-2}]$	σ_z	$\Omega_{survey}[\text{deg}^2]$	ℓ_{min}	ℓ_{max}	k_{max}	n_{bins}
0.9	30	0.05	15000	10	1000	1.0	10

4.3 Scales considered and non-linear corrections

The cuts in angular and radial scales that we perform, $\ell_{max} = 1000$ and $k_{max} = 1.0\,\text{h}\,\text{Mpc}^{-1}$, are such that we avoid the deeply non-linear regime of structure growth. We demonstrate this point in Fig. 1, showing the signal and noise parts of the covariance matrices (12 and 17) for two ℓ-modes, 10 and 1000, which correspond to the minimum and maximum multipole considered in our analysis, respectively. We notice how even for the higher ℓ case, the range of k scales considered justifies our choice to use the linear power spectrum for our analysis, since the higher k part of the spectrum is dominated by the noise (notice the different orders of magnitude between the signal and noise contributions). In Fig. 2 we plot only the diagonal contributions to the covariance matrices, distinguishing between the signal and noise parts, for $\ell = 10$ and $\ell = 1000$, our minimum and maximum angular multipoles. One can see how the orders of magnitude of the covariance matrices between different multipoles change and also how the dominance of the signal over the noise part gets inverted going from low- to high-ℓ values.

We compare forecasts obtained with a linear matter power spectrum in the calculation of the shear covariances to those obtained with a non-linear power spectrum. The current lack of solid understanding for non-linear corrections, in ΛCDM and even more in a modified gravity context, implies that any non-linear prescription should be employed with caution. The matter power spectra are produced using the HI_CLASS code (Zumalacárregui et al. 2016), a modification of the CLASS Boltzmann solver (Lesgourgues 2011) for Horndeski theories of gravity. In particular, hi_class allows the user to choose the parametrization for the $\alpha(\tau)$ functions which traces the evolution of the dark energy component, and the code then takes as input the proportionality coefficients $\hat{\alpha}$ (4). The choice for the fiducial values of $\hat{\alpha}_B$ and $\hat{\alpha}_M$, reported in Table 2, is close enough to ΛCDM to represent General Relativity with an additional cosmological constant, without incurring in numerical difficulties in HI_CLASS, if the $\hat{\alpha}$ coefficients are all set to zero exactly. Since HI_CLASS is a linear code it produces linearly evolved power spectra only. Non-linear corrections can however be incorporated by applying a non-linear transfer function using HALOFIT (Smith et al. 2003; Bird, Viel & Haehnelt 2012; Takahashi et al. 2012) as implemented in HI_CLASS or a more state-of-the-art version, HMCODE, developed by Mead et al. (2015), which we employ for our non-linear forecasts. Both HALOFIT and HMCODE however deal with non-linearities only in a setting where standard General Relativity is true. In order to get consistent constraints we therefore follow Alonso et al. (2016) and introduce a screening mechanism to recover General Relativity on small scales by a phenomenological modification of the $\alpha(\tau)$ functions, employing a Gaussian kernel in Fourier space
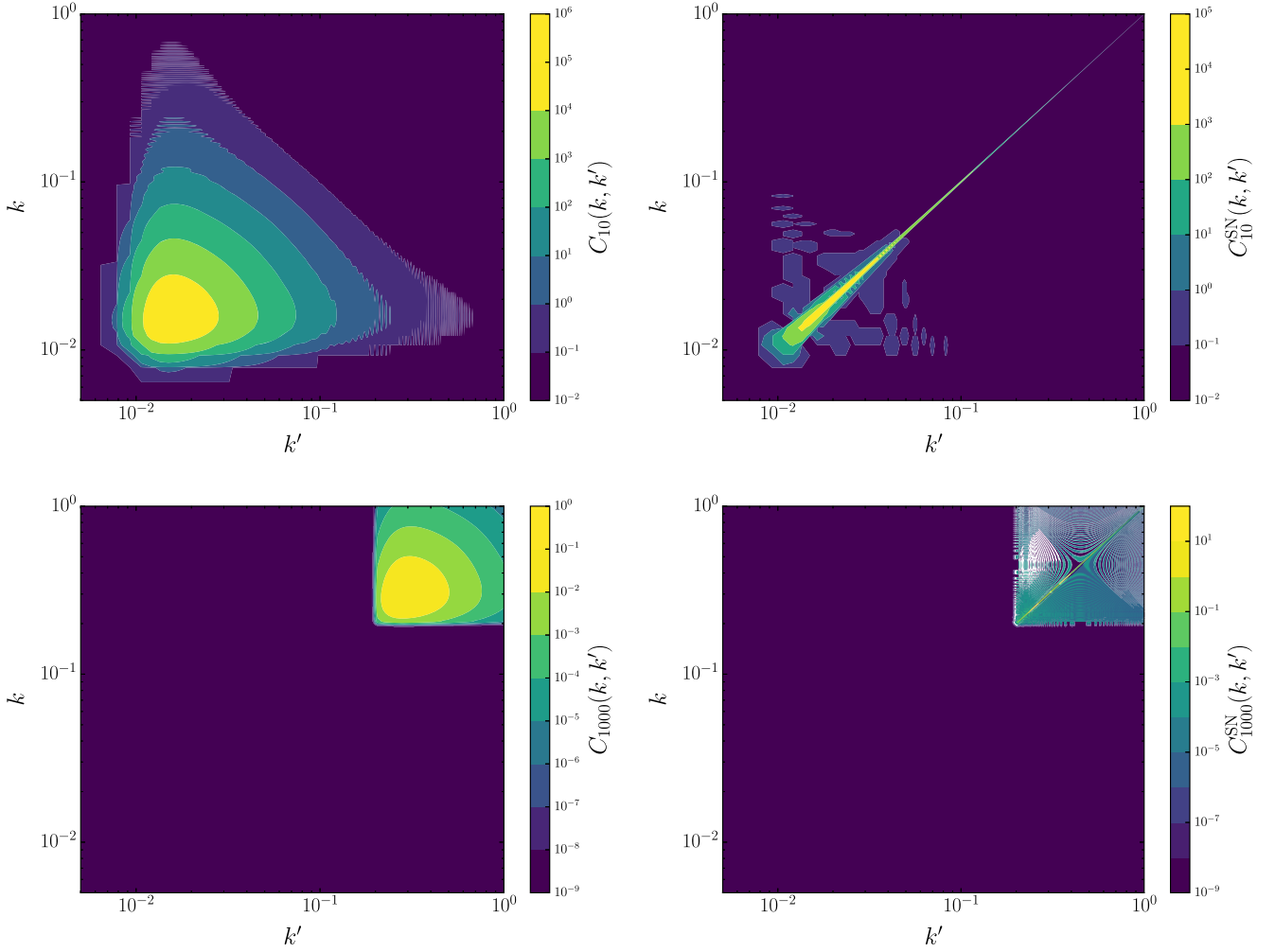
Figure 1. Signal (*left*, labelled C_ℓ) and noise (*right*, labelled $C_\ell^{\rm SN}$, where the subscript stands for shot noise) parts of the covariance matrix (12 and 17, respectively) for the minimum and maximum ℓ-mode considered in the analysis, $\ell = 10$ (*upper panels*) and $\ell = 1000$ (*bottom panels*), respectively. Note the different ranges of the colour bars, in logarithmic scale. See also Fig. 2 for a comparison between the diagonal elements of the matrices, highlighting how different multipoles have contributions with different orders of magnitude and how the signal and noise parts become dominant for low- and high-ℓ values, respectively.

with a characteristic scale k_V:

$$\alpha(\tau) \rightarrow \alpha(\tau, k) = \alpha(\tau) \exp\left(-\frac{1}{2}\left(\frac{k}{k_V}\right)^2\right). \qquad (27)$$

We marginalize over the scale $k_V = 0.1\,{\rm h\,Mpc}^{-1}$ at which the screening mechanism becomes effective. The fiducial choice for the screening is important in the sense that non-linear effects become important at scales smaller than $0.1\,{\rm h\,Mpc}^{-1}$. Additionally, Barreira et al. (2013) showed that the typical scale of Vainshtein screening is roughly at $0.1\,{\rm h\,Mpc}^{-1}$. A plot with two different choices of k_V can be found in Appendix B.

5 RESULTS

In this section we will investigate the signal strength of a weak lensing analysis carried out using the full photometric redshift information via the 3D method as well as by using a tomographic technique. As already mentioned we calculate the tomographic lensing power spectrum using the Limber approximation; for a more detailed discussion we refer to Kitching et al. (2016a). We then

show the possible constraints on Horndeski cosmological models with survey specifications given in Table 1.

5.1 Signal to noise for 3D and tomographic weak lensing

Fig. 3 shows the differential signal-to-noise (SNR) curve for a tomographic survey relative to a 3D analysis as a function of the number of tomographic bins. The total signal-to-noise ratio is calculated as

$$\Sigma^2(\leq \ell) = f_{\rm sky} \sum_{\ell'=\ell_{\rm min}}^{\ell} \frac{2\ell'+1}{2} {\rm Tr}\left[\boldsymbol{C}_{\ell'}^{-1}\boldsymbol{S}_{\ell'}\boldsymbol{C}_{\ell'}^{-1}\boldsymbol{S}_{\ell'}\right]$$

$$\equiv \sum_{\ell'=\ell_{\rm min}}^{\ell} \Delta\Sigma^2(\ell'), \qquad (28)$$

where $\boldsymbol{S}$ is the signal covariance (12) or (18) only, while $\boldsymbol{C}$ refers to the sum of signal and noise, i.e. (12) and (17), or (20).

The number of tomographic redshift bins is shown in the colour bar. Clearly an increase in the number of bins used increases the SNR, however, the gain in signal saturates for $n_{\rm bins} \approx 15$ due to
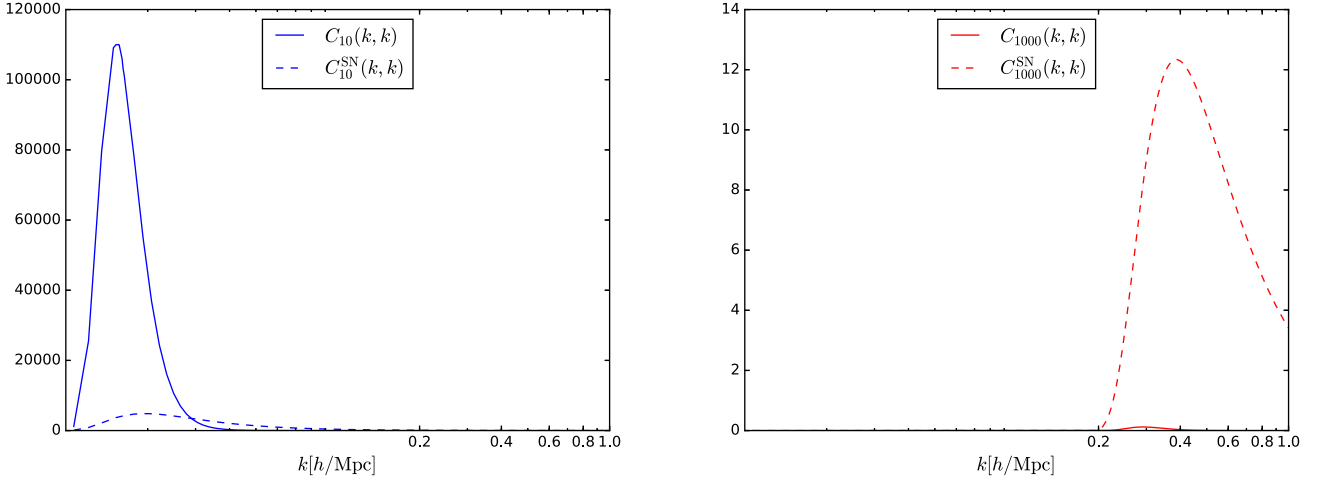
Figure 2. Comparison between the diagonal elements of the signal (*solid line*, as given by (12) and labelled C_ℓ) and noise (*dashed line*, as given by (17) and labelled C_ℓ^{SN}, where the subscript stands for shot noise) contributions to the covariance matrices of the shear modes, for the minimum and maximum angular multipole considered in this analysis, i.e. $\ell = 10$ (*blue*) and $\ell = 1000$ (*red*), respectively. Note the different orders of magnitude for the different multipoles, and how the signal prevails on the noise for low multipoles, while the noise dominates for higher ℓ values. Note also the log-scale on the x-axis to help identify the different k-regions, where most of the contributions come from for different multipoles.

Table 2. Marginalized errors $\sigma_i = \left[(\boldsymbol{F}^{-1})_{ii}\right]^{1/2}$ for the survey characteristics from Table 1. We compare a tomographic analysis with the 3D analysis using a linear power spectrum. Furthermore the influence of the value $\hat{\alpha}_K$ is investigated. Lastly the impact of non-linear clustering is quantified. When reporting the relative percentage error for the $\hat{\alpha}$ coefficients, we calculate it with respect to their fiducial values increased by one, as they are indeed expected to be $O(1)$ if one assumes the parametrization tracing the dark energy density fraction to model the time evolution of the $\hat{\alpha}(\tau)$ functions (Bellini et al. 2016).

	$\hat{\alpha}_K$	$\hat{\alpha}_B$	$\hat{\alpha}_M$	$\hat{\alpha}_T$	Ω_m	σ_8	h	n_s	Ω_b	$\sum m_\nu$
Fiducial value	0.01	0.05	0.05	0.05	0.314	0.834	0.678	0.968	0.0486	0.05
Error 3DWL linear, varying $\hat{\alpha}_K$ (fiducial value 0.01), varying $\hat{\alpha}_T$ (fiducial value 0.05)	137 (13 564%)	0.82(78%)	2.24 (213%)	5.62(535%)	0.015 (4.78%)	0.045 (5.39%)	0.307 (45.28%)	0.101 (10.43%)	0.027 (55.55%)	0.484 (968%)
Error tomography linear, $\hat{\alpha}_K = 0.01, \hat{\alpha}_T = 0$	–	0.57 (54%)	1.66 (158%)	–	0.017 (5.41%)	0.056 (6.71%)	0.257 (37.90%)	0.088 (9.09%)	0.022 (45.27%)	0.472 (944%)
Error 3DWL linear, $\hat{\alpha}_K = 0.01, \hat{\alpha}_T = 0$	–	0.43 (41%)	1.32 (126%)	–	0.013 (4.14%)	0.042 (5.03%)	0.239 (35.25%)	0.080 (8.26%)	0.021 (43.21%)	0.408 (816%)
Error 3DWL linear, $\hat{\alpha}_K = 10, \hat{\alpha}_T = 0$	–	0.48 (46%)	1.40 (133%)	–	0.014 (4.46%)	0.043 (5.15%)	0.238 (35.10%)	0.080 (8.26%)	0.021 (43.21%)	0.400 (800%)
Error 3DWL non-linear, $\hat{\alpha}_K = 0.01, \hat{\alpha}_T = 0$	–	0.25 (24%)	0.55 (52%)	–	0.011 (3.50%)	0.010 (1.20%)	0.134 (19.76%)	0.038 (3.92%)	0.016 (32.92%)	0.229 (458%)

the non-vanishing cross-correlation between the different bins. It should be noted that there is in principle an additional effect due to the finite width of the photometric redshift estimation. If the average bin width in the tomographic case is of the order of the width of the distribution of redshift estimation error, the correlation between neighbouring bins will be underestimated, thus artificially producing signal. This effect is, however, very small as long as σ_z is sufficiently small. In the 3D case this correlation is represented by the covariance (12).

Fig. 4 displays the impact of non-linear clustering: if one only considers linear structure growth (dashed line), the shot noise starts dominating the signal at $\ell \approx 450$. For the non-linear power spectrum instead the differential signal-to-noise rises until $\ell \approx 1000$ (solid line) due to the enhancement of small-scale structure by non-linear clustering. This shows the importance of the inclusion of high multipoles into the analysis. More specifically, we see that

the non-linear effects become important already at a relatively low $\ell \lesssim 200$.

5.2 Cosmological constraints on Horndeski functions

In our forecasts we fix α_T very close to zero and do not consider it as a parameter in our Fisher matrix analysis, reflecting the recent very strong constraints on the gravitational waves speed set by the detection of the binary neutron star merger GW170817 and the gamma ray burst GRB170817A (Abbott et al. 2017a,b; Baker et al. 2017; Creminelli & Vernizzi 2017; Ezquiaga & Zumalacárregui 2017; Sakstein & Jain 2017). Furthermore the kineticity α_K is largely unconstrained by cosmological observables (Alonso et al. 2016; Bellini et al. 2016), therefore we fix the coefficient $\hat{\alpha}_K$ to its fiducial value. However, we study the impact of the choice of $\hat{\alpha}_K$ on the
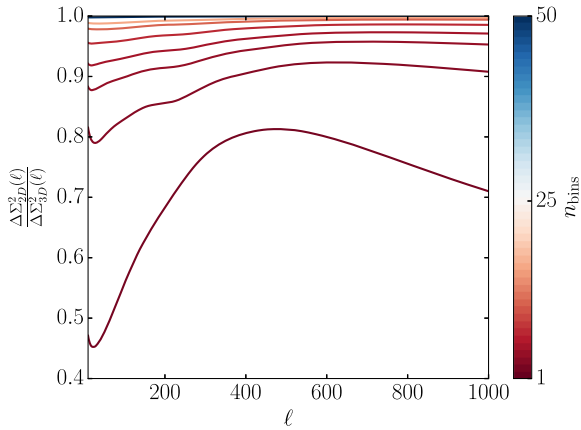
Figure 3. Differential signal-to-noise ratio of a tomographic analysis relative to a 3D analysis. The number of tomographic bins is shown in the colour bar.
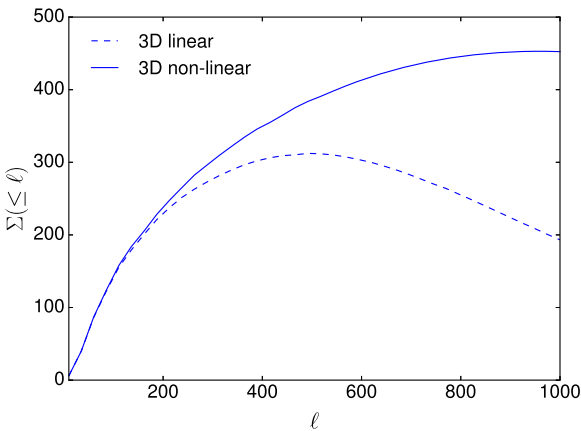

Figure 4. Differential signal-to-noise ratio, (28), i.e. Σ^2 gained at each multipole ℓ: impact of the non-linear power on the 3D lensing signal. The solid curve shows the differential signal-to-noise with a non-linear power spectrum, while the dashed curve refers to a linear one.
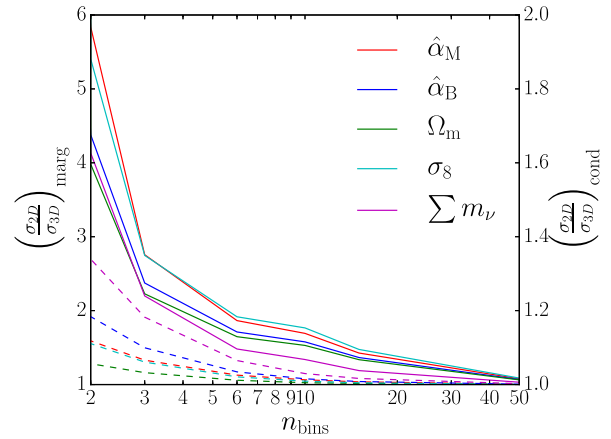

Figure 5. Errors on different parameters from a tomographic analysis relative to a 3D analysis as a function of the number of tomographic bins, n_{bins} (in log-scale on the x-axis). The solid lines show the ratio of the marginal errors belonging to the left y-axis, while the dashed lines show the conditional errors belonging to the right y-axis.

Fig. 6 shows a comparison between cosmological constraints obtained with 3D cosmic shear and tomography with specifications from Table 1. Constraints from a 3D analysis are tighter than those from tomography, due to the increased redshift information. Furthermore, the degeneracies are in all cases very similar for the two methods, which is expected since the two methods probe the same quantity. In particular we find the usual degeneracy in Ω_m and σ_8, which is slightly reduced in the 3D case. Generally, the biggest improvement can be seen for parameters carrying information about the background evolution and the growth of structures; in contrast, parameters such as the spectral index n_s are not that much influenced.

In Fig. 7, instead, we study the impact of the choice of $\hat{\alpha}_K$ and compare constraints obtained only with 3D cosmic shear using a linear matter power spectrum, but with two different choices of fixed $\hat{\alpha}_K$, namely $\hat{\alpha}_K = 0.01$ and $\hat{\alpha}_K = 10$. We find, in agreement with Alonso et al. (2016), that the choice of $\hat{\alpha}_K$ does not affect the large-scale structure observables significantly. Since the largest effect on structure formation of $\hat{\alpha}_K$ comes from very large scales beyond those considered in this work, we do not expect any significant dependence of the Fisher matrix on this parameter.

Finally we investigate the impact of non-linear clustering in Fig. 8 as outlined before. Constraints are, as expected, tighter with the addition of the non-linear corrections. In particular, we find a significant gain in Ω_m, σ_8, and $\sum m_\nu$[eV]. Other parameters such as the spectral index n_s and the Hubble constant h are not that much affected, since the main characteristics are already captured in the linear power spectrum. Furthermore we find a gain in sensitivity in $\hat{\alpha}_B$ and $\hat{\alpha}_M$. This reduction of the error for the modified gravity parameters is mainly due to the marginalization process and the degeneracies with the other parameters such as Ω_m, which are better constrained now. In fact, it should be noted that the conditional constraints on $\hat{\alpha}_M$ and $\hat{\alpha}_B$ become slightly worse than in the linear case, which has a subtle reason: the screening scale is chosen such that modified gravity effects are suppressed as soon as non-linear effects set in, on the other hand however, there is loss of power on intermediate scales. This effectively yields a loss in sensitivity, since the full effect of modified gravity is only present up to intermediate scales, whereas the signal gain on small scales does not contribute to the Fisher matrix. Finally, as a consequence of the screening
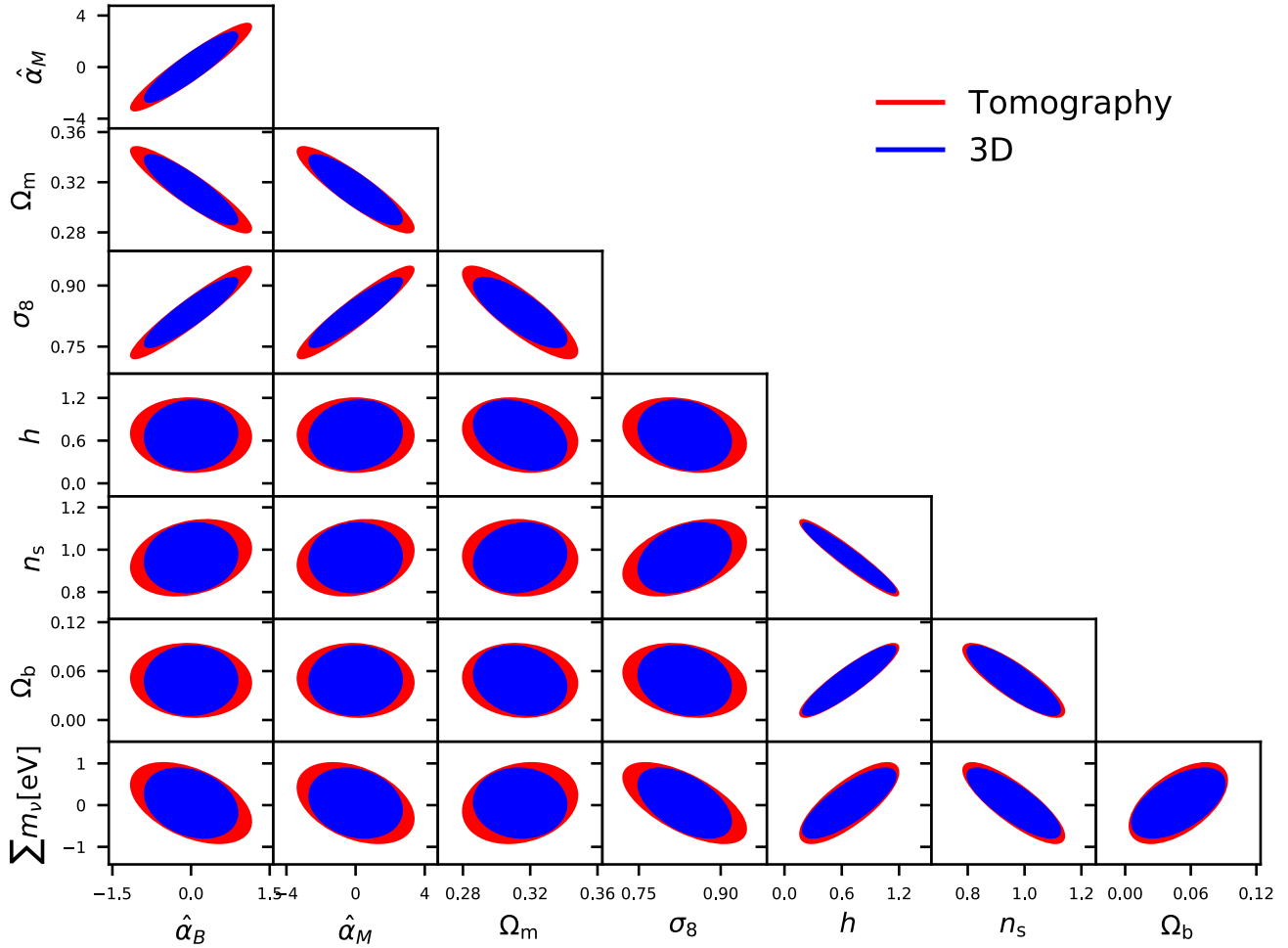
constraints on the other parameters by choosing two values which differ by three orders of magnitude.

As already seen in Fig. 3 a lot of signal comes from non-linear scales, in fact for Euclid one expects that about two thirds of the total signal to noise, $\Sigma(< \ell_{max})$ with $\ell_{max} \approx 2000$, originate from non-linear scales. It is therefore evident that one has to include non-linear clustering in the analysis in order to get the necessary statistical power to constrain a high-dimensional parameter space.

As seen before, increasing the number of tomographic bins yields more signal. In the inference process, however, the sensitivity to the model parameters plays an important role. For linear model parameters one expects the sensitivity to be a rescaled version of the SNR curve. In Fig. 5 we show the marginal and conditional errors of a tomographic analysis relative to the 3D analysis for a few parameters. The marginal errors are more strongly affected, since the contributions from the conditional errors add up during the marginalization procedure. Furthermore, we see the same trend as for the SNR: the expected errors tend towards the errors of a 3D analysis for $n_{bins} \gg 1$.

Figure 6. 1σ forecast contours for a Euclid-like survey, showing a comparison between a fully 3D (*blue*) and a tomographic cosmic shear analysis (*red*). The fiducial values can be found in Table 2, while $\hat{\alpha}_K = 0.01$ and the survey specifications are given in Table 1. We used the linear matter power spectrum for both.

mechanism, the orientation of the ellipses, for example, in the case $\Omega_m - \hat{\alpha}_M$ and $\sigma_8 - \hat{\alpha}_M$, can change; this is due to the increase in signal at high-ℓ values and the change of the sensitivity to cosmological parameters, especially because the sensitivity to the modified gravity parameters on those scales vanishes by construction.

In order to exploit the full potential of non-linear clustering, one would need to have a reliable model for non-linear structure formation in a modified gravity setting. The way it is presented here effectively assumes that modifications of the gravitational field equation only play a role at linear order, while higher orders are treated in the usual framework of perturbation theory in a ΛCDM cosmology.

6 DISCUSSION AND CONCLUSIONS

In this work we investigated the performance of a 3D analysis of cosmic shear measurements as a probe of Horndeski theories of modified gravity. We set constraints by means of a Fisher matrix analysis on a set of parameters that completely describe the evolution of linear perturbations in Horndeski gravity, using the specifications of a future Euclid-like experiment. We placed simultaneously our constraints on both the modified gravity parameters and on a set of standard cosmological parameters, including the sum of neutrino masses. Analogous forecasts for a tomographic analysis

with six bins were produced given the same specifications of the cosmic shear experiment, with the aim of comparing the two methods. Our analysis was restricted to angular modes $\ell \leq 1000$ and $k \leq 1\,h\,\mathrm{Mpc}^{-1}$, to avoid the deeply non-linear regime of structure growth. We summarize our results as follows.

The signal-to-noise ratio of both a 3D analysis and a tomographic one is very similar, since it is mainly driven by the amplitude of the lensing signal and a tomographic method effectively agrees with a decomposition into spherical harmonics and radial Bessel functions if the bin width gets as small as the width of the photometric redshift errors.

3D cosmic shear provides tighter constraints than 10 bins tomography. Even with our conservative cut in angular and radial scales and using a linear matter power spectrum for the calculation of the covariance of the shear modes, 3D weak lensing performs better than tomography for all cosmological parameters, with both methods showing very similar degeneracies. For the parameters of Bellini and Sawicki (2014) parametrization describing Horndeski theories, the gain is of the order of roughly 20 per cent in the errors.

We investigated the impact of the fiducial value chosen for the kineticity and found that the constraints are largely unaffected by the choice of $\hat{\alpha}_K$. In particular we used $\hat{\alpha}_K = 0.01$ and $\alpha_K = 10$.

To illustrate the importance of non-linear corrections, we showed the expected improvement in the size of the constraints obtained
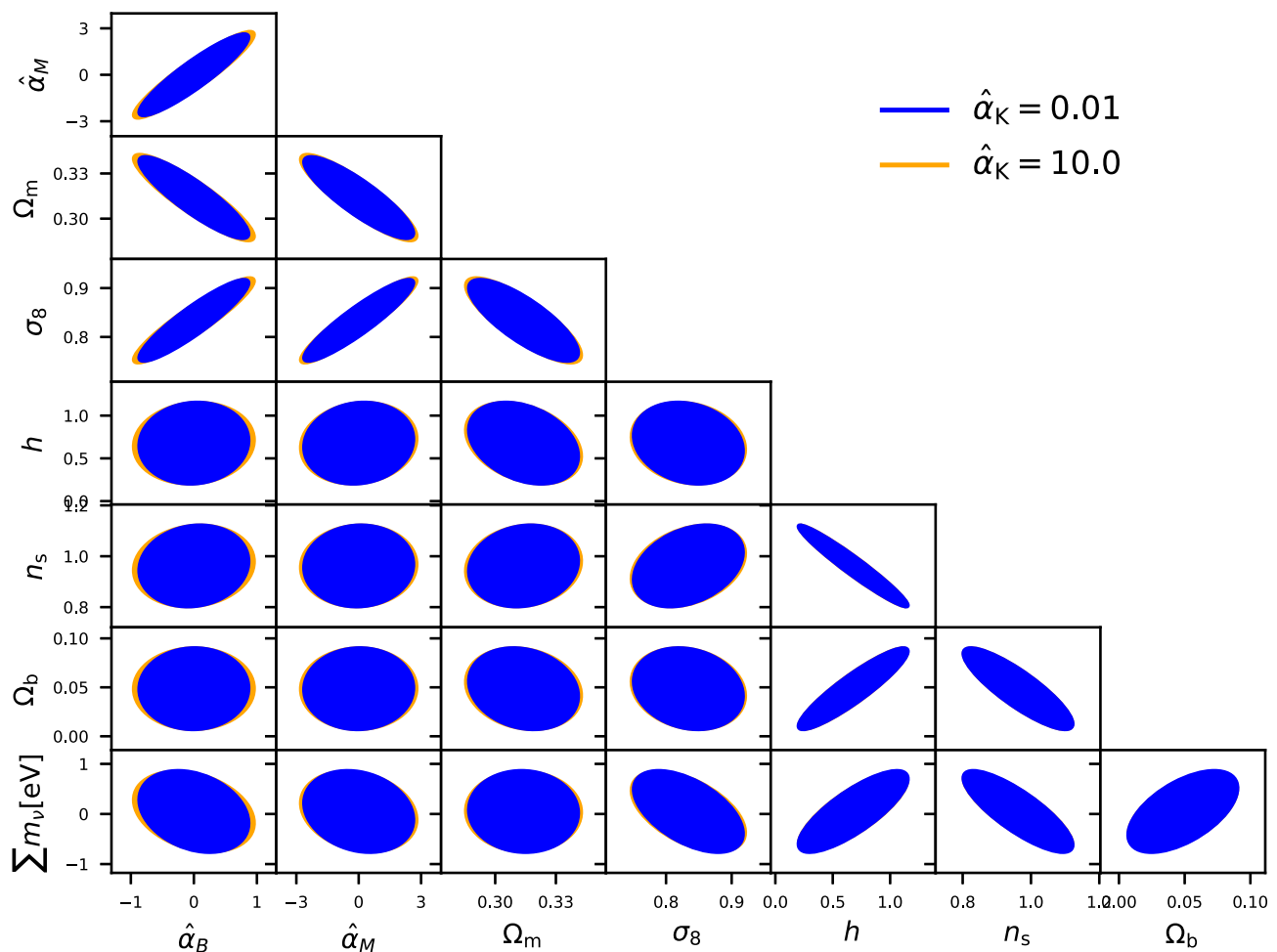
Figure 7. Impact of the choice of $\hat{\alpha}_K$ for a 3D cosmic shear analysis with fiducial values from Table 2 and survey specifications given in Table 1. We used a linear power spectrum for the analysis and show the difference in the 1σ contours when fixing $\hat{\alpha}_K = 0.01$ (*blue*) or $\hat{\alpha}_K = 10$ (*orange*).

employing a non-linear matter power spectrum: the results obtained in this case serve as an illustrative example of the constraining power of non-linear scales. In order to obtain a complete and self-consistent picture, one would need a formalism to construct the non-linear corrections in a general modified gravity setting (see e.g. Lombriser 2016; Fasiello & Vlah 2017). Here we introduced an artificial screening scale, which pushes the deviations from General Relativity to zero below its value. This is, however, not a fully exhaustive ansatz and many more investigations in this direction are required. The gain in signal if non-linear clustering is considered clearly shows the importance and calls for the development of analytic or semi-analytic prescriptions for the treatment of non-linear scales in ΛCDM and modified gravity. These will play a crucial role in allowing cosmic shear measurements to set strong constraints on parameters describing deviations from General Relativity. Due to the screening the constraints on modified gravity parameters are only improved because of the marginalization over the remaining parameters.

Compared to the analysis of Pratten et al. (2016), our study extends the scope to the full Horndeski class and we do not fix all the parameters describing the background to their ΛCDM values. This large parameter space and the fact that we only

considered weak gravitational lensing as our observable makes our constraints less tight than the ones presented in Alonso et al. (2016), given also that our range in scales is less extended. Additionally, we present a 3D analysis along with a tomographic one, showing the increase in sensitivity of the former.

In our analysis we did not consider spurious contributions to the pure lensing signal coming from systematics such as the intrinsic alignments of source galaxies (Joachimi & Bridle 2010; Mandelbaum 2017). These are expected to dominate the error budget for future cosmic shear surveys and need therefore to be carefully accounted for. These contributions are also expected to influence mostly the lensing signal on small, non-linear scales. The scales we considered were also chosen with the purpose of avoiding the regime of domination of these effects, which we considered neither in our fully 3D approach nor in the tomographic one, so that the comparison could remain fair. However, it has been shown that this kind of systematics can be carefully accounted for in 3D analyses (Merkel & Schäfer 2013) and we plan to investigate their impact in future work, together with cross-correlations with other probes which we envisage as one of the most powerful tools to test gravity on cosmological scales.
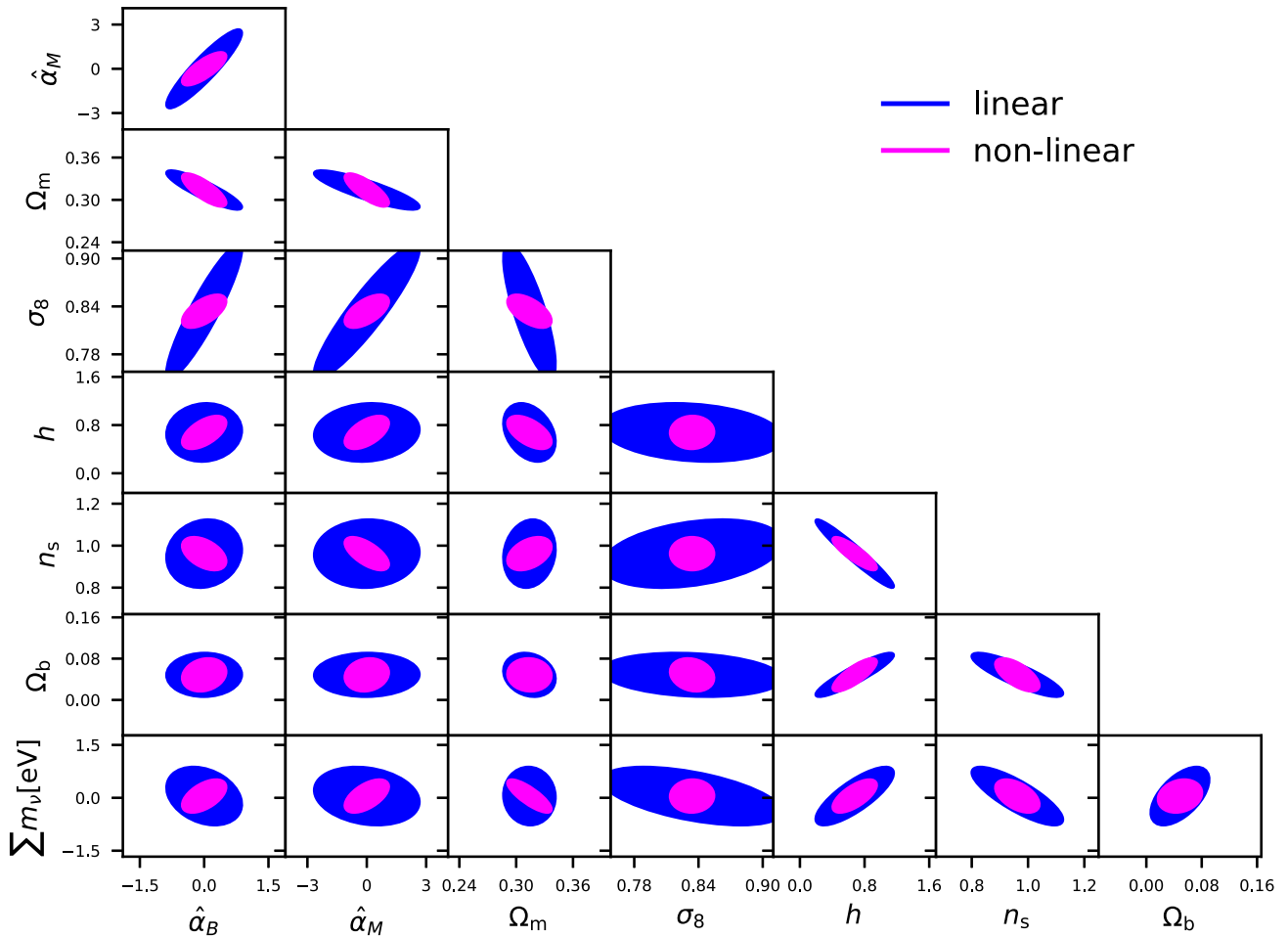
Figure 8. Impact of non-linear clustering with fiducial values from Table 2 and survey specifications are given in Table 1. We show the constraints obtained with the linear power spectrum in *blue* and with the non-linear one in *magenta*.

REFERENCES

Abbott B. P. et al., 2017a, Phys. Rev. Lett., 119, 161101
Abbott B. P. et al., 2017b, ApJ, 848, 59
Abramowitz M., Stegun I. A., Romer R. H., 1988, Am. J. Phys., 56, 958
Adamek J., Durrer R., Tansella V., 2016, J. Cosmol. Astropart. Phys., 1, 024
Alonso D., Bellini E., Ferreira P. G., Zumalacarregui M., 2016, Phys. Rev. D, 95, 063502
Amendola L., Kunz M., Sapone D., 2008, J. Cosmol. Astropart. Phys., 4, 013
Amendola L. et al., 2016, Living Rev. Relativ. 21, 34
Armendáriz-Picón C., Damour T., Mukhanov V., 1999, Phys. Lett. B, 458, 209
Armendariz-Picon C., Mukhanov V., Steinhardt P. J., 2001, Phys. Rev. D, 63, 103510
Ayaita Y., Schäfer B. M., Weber M., 2012, MNRAS, 422, 3056
Bacon D. J., Refregier A. R., Ellis R. S., 2000, MNRAS, 318, 625

Baker T., Bull P., 2015, ApJ, 811, 116
Baker T., Bellini E., Ferreira P. G., Lagos M., Noller J., Sawicki I., 2017, Phys. Rev. Lett., 119, 251301
Barreira A., Li B., Hellwing W. A., Baugh C. M., Pascoli S., 2013, J. Cosmol. Astropart. Phys., 10, 027
Bartelmann M., Schneider P., 2001, Phys. Rep., 340, 291
Bellini E., Sawicki I., 2014, J. Cosmol. Astropart. Phys., 2014, 050
Bellini E., Cuesta A. J., Jimenez R., Verde L., 2016, J. Cosmol. Astropart. Phys., 2, 053
Bernstein G., Jain B., 2004, ApJ, 600, 17
Bettoni D., Liberati S., 2013, Phys. Rev. D, 88, 084020
Bettoni D., Ezquiaga J. M., Hinterbichler K., Zumalacárregui M., 2017, Phys. Rev. D, 95, 084029
Bird S., Viel M., Haehnelt M. G., 2012, MNRAS, 420, 2551
Brans C., Dicke R. H., 1961, Phys. Rev., 124, 925
Brown M. L., Taylor A. N., Bacon D. J., Gray M. E., Dye S., Meisenheimer K., Wolf C., 2003, MNRAS, 341, 100
Camera S., Kitching T. D., Heavens A. F., Bertacca D., Diaferio A., 2011, MNRAS, 415, 399
Carroll S. M., Duvvuri V., Trodden M., Turner M. S., 2004, Phys. Rev. D, 70, 043528
Carroll S. M., de Felice A., Duvvuri V., Easson D. A., Trodden M., Turner M. S., 2005, Phys. Rev. D, 71, 063513
Castro P. G., Heavens A. F., Kitching T. D., 2005, Phys. Rev. D, 72, 023516
Charmousis C., Copeland E. J., Padilla A., Saffin P. M., 2012, Phys. Rev. Lett., 108, 051101
Clerkin L. et al., 2017, MNRAS, 466, 1444

Clifton T., Ferreira P. G., Padilla A., Skordis C., 2012, Phys. Rep., 513, 1
Creminelli P., Vernizzi F., 2017, Phys.Rev. Lett., 119, 251302
Crisostomi M., Koyama K., 2017, Phys. Rev. D, 97, 084004
de Rham C., Gabadadze G., 2010, Phys. Rev. D, 82, 044020
de Rham C., Tolley A. J., 2010, J. Cosmol. Astropart. Phys., 5, 015
de Rham C., Gabadadze G., Tolley A. J., 2011, Phys. Rev. Lett., 106, 231101
Deffayet C., Esposito-Farèse G., Vikman A., 2009, Phys. Rev. D, 79, 084003
Deffayet C., Pujolàs O., Sawicki I., Vikman A., 2010, J. Cosmol. Astropart. Phys., 10, 026
Deffayet C., Gao X., Steer D. A., Zahariade G., 2011, Phys. Rev. D, 84, 064039
Durrer R., Tansella V., 2016, J. Cosmol. Astropart. Phys., 7, 037
Ezquiaga J., Zumalacárregui M., 2017, Phys. Rev. Lett., 119, 251304
Ezquiaga J., García-Bellido J., Zumalacárregui M., 2016, Phys. Rev. D, 94, 024005
Fasiello M., Vlah Z., 2017, Phys. Lett., B773, 236
Gleyzes J., 2017, Phys. Rev. D, 96, 063516
Gleyzes J., Langlois D., Piazza F., Vernizzi F., 2013, J. Cosmol. Astropart. Phys., 8, 025
Gleyzes J., Langlois D., Piazza F., Vernizzi F., 2015, Phys. Rev. Lett., 114, 211101
Goldberg J. N., Macfarlane A. J., Newman E. T., Rohrlich F., Sudarshan E. C. G., 1967, J. Math. Phys., 8, 2155
Grassi A., Schäfer B. M., 2014, MNRAS, 437, 2632
Gubitosi G., Piazza F., Vernizzi F., 2013, J. Cosmol. Astropart. Phys., 2, 032
Hannestad S., Tu H., Wong Y. Y., 2006, J. Cosmol. Astropart. Phys., 6, 025
Hassan S. F., Rosen R. A., 2012, J. High Energy Phys., 2, 126
Heavens A., 2003, MNRAS, 343, 1327
Heavens A. F., Kitching T. D., Taylor A. N., 2006, MNRAS, 373, 105
Heymans C. et al., 2013, MNRAS, 432, 2433
Hinterbichler K., Khoury J., 2010, Phys. Rev. Lett., 104, 231301
Hinterbichler K., Khoury J., Levy A., Matas A., 2011, Phys. Rev. D, 84, 103521
Hoekstra H., Jain B., 2008, Annu. Rev. Nucl. Part. Sci., 58, 99
Hollenstein L., Sapone D., Crittenden R., Schäfer B. M., 2009, J. Cosmol. Astropart. Phys., 4, 012
Horndeski G. W., 1974, Int. J. Theor. Phys., 10, 363
Hu W., 1999, ApJ, 522, L21
Huterer D., 2010, Gen. Relativ. Gravit., 42, 2177
Jacobson T., Mattingly D., 2001, Phys. Rev. D, 64, 024028
Jain B., Seljak U., 1997, ApJ, 484, 560
Jain B., Taylor A., 2003, Phys. Rev. Lett., 91, 141302
Jee M. J., Tyson J. A., Schneider M. D., Wittman D., Schmidt S., Hilbert S., 2013, ApJ, 765, 74
Joachimi B., Bridle S. L., 2010, A&A, 523, A1
Joachimi B., Taylor A. N., Kiessling A., 2011, MNRAS, 418, 145
Joyce A., Lombriser L., Schmidt F., 2016, Annu. Rev. Nucl. Part. Sci., 66, 95
Kaiser N., 1992, ApJ, 388, 272
Kaiser N., 1998, ApJ, 498, 26
Khoury J., Weltman A., 2004a, Phys. Rev. D, 69, 044026
Khoury J., Weltman A., 2004b, Phys. Rev. Lett., 93, 171104
Kilbinger M., 2015, Rep. Prog. Phys., 78, 086901
Kilbinger M. et al., 2009, A&A, 497, 677
Kilbinger M. et al., 2013, MNRAS, 430, 2200
Kilbinger M. et al., 2017, MNRAS, 472, 2126
Kitching T. D., Heavens A. F., 2017, Phys. Rev. D, 95, 063522
Kitching T. D., Heavens A. F., Taylor A. N., Brown M. L., Meisenheimer K., Wolf C., Gray M. E., Bacon D. J., 2007, MNRAS, 376, 771
Kitching T. D., Heavens A. F., Miller L., 2011, MNRAS, 413, 2923
Kitching T. D. et al., 2014, MNRAS, 442, 1326
Kitching T. D., Alsing J., Heavens A. F., Jimenez R., McEwen J. D., Verde L., 2016a, MNRAS, 469, 2737
Kitching T. D., Verde L., Heavens A. F., Jimenez R., 2016b, MNRAS, 459, 971
Kobayashi T., Yamaguchi M., Yokoyama J., 2010, Phys. Rev. Lett., 105, 231302
Kreisch C. D., Komatsu E., 2017, preprint (arXiv:1712.02710)
Langlois D., Mancarella M., Noui K., Vernizzi F., 2017, J. Cosmol. Astropart. Phys., 5, 033
Laureijs R. et al., 2011, preprint (arXiv:1110.3193)
Lemos P., Challinor A., Efstathiou G., 2017, J. Cosmol. Astropart. Phys., 5, 014
Lesgourgues J., 2011, preprint (arXiv:1104.2932)
Lombriser L., 2016, J. Cosmol. Astropart. Phys., 11, 039
Lombriser L., Lima N. A., 2017, Phys. Lett. B, 765, 382
Loverde M., Afshordi N., 2008, Phys. Rev. D, 78, 123506
LSST Science Collaboration, 2009, preprint (arXiv:0912.0201)
Maartens R., Abdalla F. B., Jarvis M., Santos M. G., SKA Cosmology SWG, 2015, preprint (arXiv:1501.04076)
Mandelbaum R., 2018, preprint (arXiv:1710.03235, Annual Review of Astronomy and Astrophysics, 56, 1)
Martin J., 2012, C. R. Phys., 13, 566
Martín-Moruno P., Nunes N. J., Lobo F. S. N., 2015, Phys. Rev. D, 91, 084029
Mead A. J., Peacock J. A., Heymans C., Joudaki S., Heavens A. F., 2015, MNRAS, 454, 1958
Merkel P. M., Schäfer B. M., 2013, MNRAS, 434, 1808
Munshi D., Kilbinger M., 2006, A&A, 452, 63
Newman E., Penrose R., 1962, J. Math. Phys., 3, 566
Nicolis A., Rattazzi R., Trincherini E., 2009, Phys. Rev. D, 79, 064036
Peirone S., Koyama K., Pogosian L., Raveri M., Silvestri A., 2018, Phys. Rev. D, 97, 043519
Perlmutter S. et al., 1999, ApJ, 517, 565
Planck Collaboration et al., 2016, A&A, 594, A14
Pratten G., Munshi D., Valageas P., Brax P., 2016, Phys. Rev. D, 93, 103524
Pujolàs O., Sawicki I., Vikman A., 2011, J. High Energy Phys., 11, 156
Ratra B., Peebles P. J. E., 1988, Phys. Rev. D, 37, 3406
Riess A. G. et al., 1998, AJ, 116, 1009
Sakstein J., Jain B., 2017, Phys. Rev. Lett., 119, 251303
Sawicki I., Bellini E., 2015, Phys. Rev. D, 92, 084061
Schäfer B. M., Heisenberg L., 2012, MNRAS, 423, 3445
Semboloni E., Hoekstra H., Schaye J., van Daalen M. P., McCarthy I. G., 2011, MNRAS, 417, 2020
Semboloni E., Hoekstra H., Schaye J., 2013, MNRAS, 434, 148
Simon P., King L. J., Schneider P., 2004, A&A, 417, 873
Smith R. E. et al., 2003, MNRAS, 341, 1311
Spergel D. et al., 2013, preprint (arXiv:1305.5422)
Takada M., Jain B., 2003a, MNRAS, 340, 580
Takada M., Jain B., 2003b, MNRAS, 344, 857
Takada M., Jain B., 2004, MNRAS, 348, 897
Takada M., White M., 2004, ApJ, 601, L1
Takahashi R., Sato M., Nishimichi T., Taruya A., Oguri M., 2012, ApJ, 761, 152
Taruya A., Takada M., Hamana T., Kayo I., Futamase T., 2002, ApJ, 571, 638
Tegmark M., Taylor A. N., Heavens A. F., 1997, ApJ, 480, 22
van Daalen M. P., Schaye J., Booth C. M., Dalla Vecchia C., 2011, MNRAS, 415, 3649
Van Waerbeke L. et al., 2000, A&A, 358, 30
Weinberg D. H., Mortonson M. J., Eisenstein D. J., Hirata C., Riess A. G., Rozo E., 2013, Phys. Rep., 530, 87
Wetterich C., 2009, Phys. Rev. Lett., 102, 141303
Woodard R., 2007, in Papantonopoulos L., ed., Lecture Notes in Physics, Vol. 720, The Invisible Universe: Dark Matter and Dark Energy. Springer Verlag, Berlin , p. 403
Zieser B., Merkel P. M., 2016, MNRAS, 459, 1586
Zumalacárregui M., García-Bellido J., 2014, Phys. Rev. D, 89, 064046
Zumalacárregui M., Koivisto T. S., Mota D. F., 2013, Phys. Rev. D, 87, 083010
Zumalacárregui M., , Bellini E., Sawicki I., Lesgourgues J., Ferreira P., 2016, J. Cosmol. Astropart. Phys., 8, 19

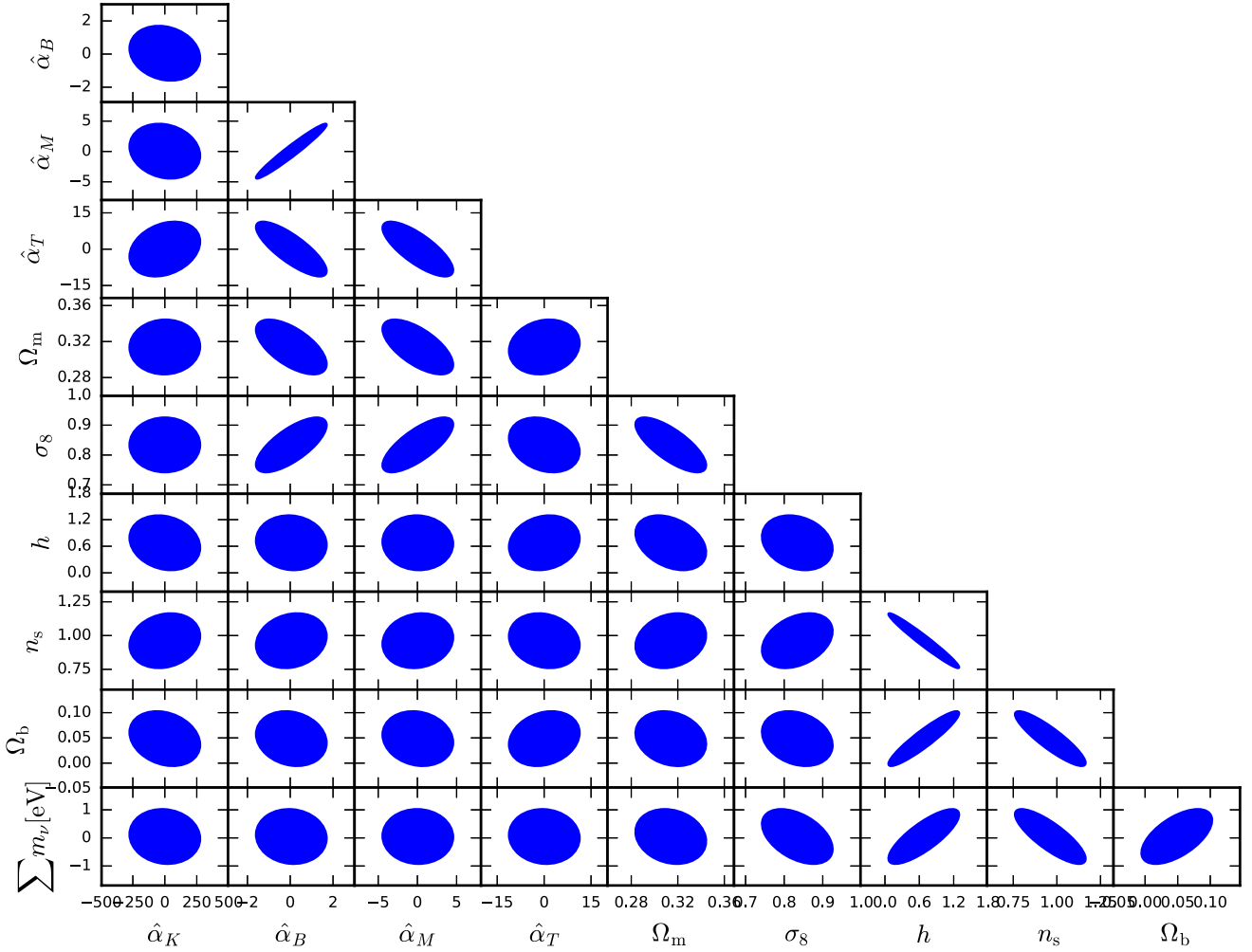**Figure A1.** Fiducial values from Table 2 and survey specifications are given in Table 1. We notice that $\hat{\alpha}_K$ is unconstrained.

APPENDIX A: VARYING $\hat{\alpha}_K$ AND $\hat{\alpha}_T$

We show in Fig. A1 the contour plots that we obtain if we also vary $\hat{\alpha}_K$ and $\hat{\alpha}_T$. We notice in particular that, as expected, $\hat{\alpha}_K$ is unconstrained therefore we decide to fix it at its fiducial value.

APPENDIX B: INFLUENCE OF k_V

In Fig. B1 we show the influence of the screening length on the constraining power. Clearly, if k_V becomes smaller, GR is retained at larger scales already, thus decreasing the sensitivity on the modified gravity parameters. For a more complete discussion we refer the reader to Alonso et al. (2016).
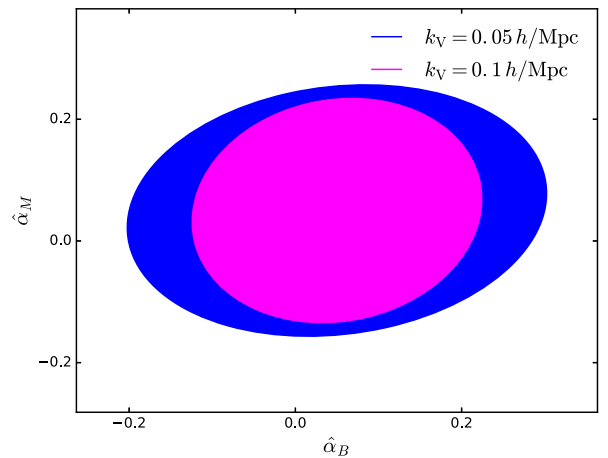

Figure B1. Constraints on $\hat{\alpha}_B$ and $\hat{\alpha}_M$ for two different choices of the screening length k_V.

This paper has been typeset from a TEX/LATEX file prepared by the author.